Rapid Communications

# Reexamining nuclear chiral geometry from the orientation of the angular momentum

Q. B. Chen (陈启博)[1] and J. Meng (孟杰)[2,3,4,*]

[1]*Physik Department, Technische Universität München, D-85747 Garching, Germany*

[2]*State Key Laboratory of Nuclear Physics and Technology, School of Physics, Peking University, Beijing 100871, China*

[3]*Yukawa Institute for Theoretical Physics, Kyoto University, Kyoto 606-8502, Japan*

[4]*Department of Physics, University of Stellenbosch, Stellenbosch, South Africa*

(Received 17 August 2018; published 26 September 2018)

The paradox on the previous interpretation for the nuclear chiral geometry based on the effective angle has been clarified by reexamining the system with the particle-hole configuration $\pi(1h_{11/2})^1 \otimes \nu(1h_{11/2})^{-1}$ and a rotor with the deformation parameter $\gamma = 30^\circ$. It is found that the paradox is caused by the fact that the angular momentum of the rotor is much smaller than those of the proton and the neutron near the bandhead. Hence, it does not support a chiral rotation interpretation near the bandhead. The nuclear chiral geometry based on the effective angle makes sense only when the angular momentum of the rotor becomes comparable with those of the proton and neutron for a particular range of spin values.

DOI: 10.1103/PhysRevC.98.031303

Chirality is a topic of general interest in the sciences, such as chemistry, biology, and physics. An object or a system is chiral if it is not identical to its mirror image, and cannot be superposed on its mirror image through any combination of rotations and translations.

The phenomenon of chirality in nuclear physics was initially introduced by Frauendorf and Meng in 1997 [1] for a fast rotating nucleus with triaxially deformed shape and high-$j$ valence particle(s) and valence hole(s). This phenomenon appears in the body-fixed reference frame where the spontaneous breaking of the chiral symmetry happens. In the laboratory reference frame, however, due to the quantum tunneling of the total angular momentum between the left- and right-handed systems, the broken chiral symmetry is restored. Then, the chiral doublet bands, i.e., a pair of nearly degenerate $\Delta I = 1$ bands with the same parity, are expected to be observed [1].

After the pioneering work on the chirality in nuclei [1], the chiral symmetry in atomic nuclei has become one of the most intriguing phenomena that has attracted significant attention and intensive studies from both experimental and theoretical sides in the last two decades. So far, more than 40 pairs of chiral doublet band candidates have been reported in the $A \approx 80$, 100, 130, and 190 mass regions. For recent reviews, see Refs. [2–8]. With the prediction [9] and confirmation [10] of multiple chiral doublets (M$\chi$D) in a single nucleus, the investigation of chirality continues to be one of the hottest topics in nuclear physics [11–29].

As demonstrated in Refs. [1,30], the chirality of nuclear rotation results from not only the static (the triaxial shape) but also the dynamic (the angular momentum) properties of the nucleus. This is quite different from the chirality in chemistry, which is of a static nature that characterizes just the geometrical arrangement of the atoms. Hence, it is of importance to examine the angular momentum geometry in order to verify whether the pair of nearly degenerated doublet bands are chiral doublet bands or not. To achieve this goal, one can investigate, for example, (1) the angular momentum components of the rotor, particle(s), and hole(s) along the three principal axes (e.g., in Refs. [1,15,16,22,31–37]); (2) the distributions of the angular momentum components on the three intrinsic axes ($K$ plot) (e.g., in Refs. [15,22,33–35,38–40]); (3) the effective angles between the angular momenta of the rotor, particle(s), and hole(s) (e.g., in Refs. [41–43]); (4) the orientation parameter of the system (e.g., in Refs. [23,41,42]); and (5) the distributions of the tilted angles of the angular momentum in the intrinsic frame (azimuthal plot) (e.g., in Refs. [39,40]).

It is known now that chiral rotation (or static chirality) can exist only above a certain critical frequency [23,31,32,44]. Namely, at low spin the chiral vibrations, understood as the oscillation of the total angular momentum between the left- and the right-handed configurations in the body-fixed frame, exists. This suggests that the orientation of the angular momenta of the rotor, particle(s), and hole(s) are *planar* at the bandhead of the chiral bands. However, it is noted that the effective angles between any two of the three angular momenta are closed to 90° as shown for the yrast band of $^{126}$Cs [43] (see also Fig. 1). This is the paradox which motivates us to reexamine the angular momentum geometries of the rotor, particle(s), and hole(s) in chiral doublet bands.

Theoretically, various approaches have been developed extensively to investigate chiral doublet bands. For example, the particle rotor model (PRM) [1,33,34,38,45–47], the titled axis cranking (TAC) model [31,32,44,48], the TAC plus random-phase approximation (RPA) [49], the collective Hamiltonian method [50,51], the interacting boson-fermion-fermion model [52], and the angular momentum projection (AMP) method [39,40,53–55]. In this work, the PRM will

*mengj@pku.edu.cn

 ©2018 American Physical Society

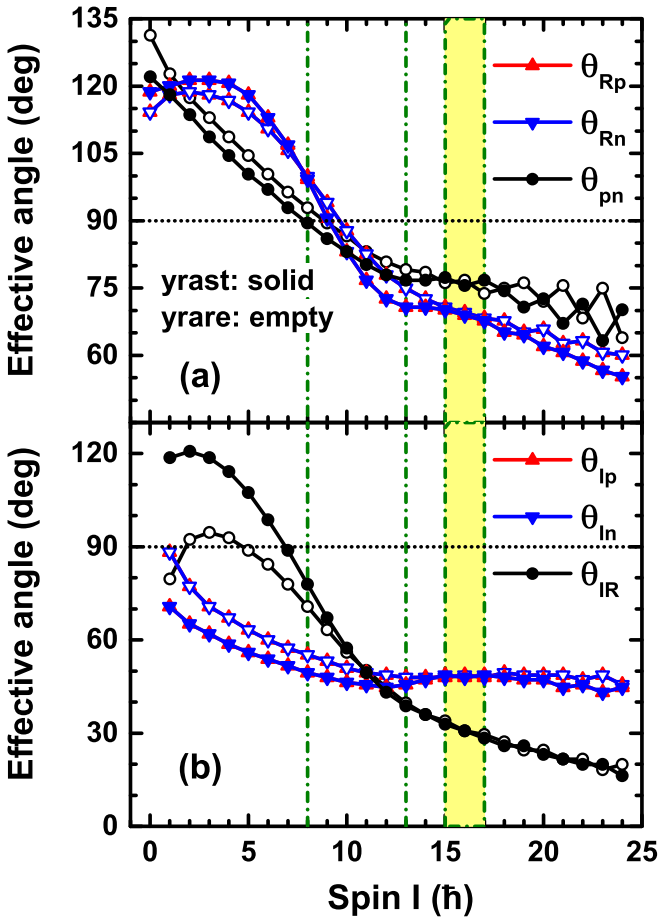


FIG. 1. Effective angles $\theta_{pn}$, $\theta_{Rp}$, $\theta_{Rn}$, $\theta_{Ip}$, $\theta_{In}$, and $\theta_{IR}$ as functions of spin for the yrast and yrare bands.

be used. The basic microscopic inputs for PRM can be obtained from the constrained covariant density functional theory (CDFT) [9,10,18,20,21,37,56]. PRM is a quantal model consisting of the collective rotation and the intrinsic single-particle motions, which describes a system in the laboratory reference frame. The total Hamiltonian is diagonalized with total angular momentum as a good quantum number. The energy splitting and quantum tunneling between the doublet bands can be obtained directly. Hence, it is straightforward to use it to investigate the angular momentum geometries of chiral doublet bands.

The detailed formalism of PRM can be found in Refs. [1,33,34,38,45]. In the calculations, a system of one $h_{11/2}$ proton particle and one $h_{11/2}$ neutron hole coupled to a triaxial rigid rotor with quadruple deformation parameters $\beta = 0.23$ and $\gamma = 30.0^\circ$ are taken as the example to illustrate the angular momentum geometry. In addition, the irrotational flow type of moments of inertia $\mathcal{J}_k = \mathcal{J}_0 \sin^2(\gamma - 2k\pi/3)$, $(k = 1, 2, 3)$ with $\mathcal{J}_0 = 30\ \hbar^2/\text{MeV}$ are used.

The effective angle $\theta_{pn}$ between the proton ($\boldsymbol{j}_p$) and neutron ($\boldsymbol{j}_n$) angular momenta is defined as [42]

$$\cos\theta_{pn} = \frac{\langle \boldsymbol{j}_p \cdot \boldsymbol{j}_n \rangle}{\sqrt{\langle \boldsymbol{j}_p^2 \rangle}\sqrt{\langle \boldsymbol{j}_n^2 \rangle}}, \tag{1}$$

and similarly for $\theta_{Rp}$, $\theta_{Rn}$, $\theta_{Ip}$, $\theta_{In}$, and $\theta_{IR}$. Here, the subscripts $p$, $n$, $R$, and $I$ denote the proton, neutron, rotor, and total spin, respectively, and $|\rangle$ is the wave function of the yrast or yrare bands. In geometry, any three vectors lie in a planar only when the sum of any two angles between the vectors equals the other one or the sum of the three angles equals 360°.

In Fig. 1, the obtained effective angles $\theta_{pn}$, $\theta_{Rp}$, $\theta_{Rn}$, $\theta_{Ip}$, $\theta_{In}$, and $\theta_{IR}$ as functions of spin for the yrast and yrare bands are presented. The dashed-dotted lines at $I =$ 8, 13, and 15–17$\hbar$ label the bandhead, the onset of aplanar rotation, and the static chirality, respectively, which are based on Figs. 2 and 3 as shown later.

From Fig. 1(a), it is observed that the effective angles $\theta_{pn}$, $\theta_{Rp}$, and $\theta_{Rn}$ are about 120° around $I = 0\hbar$, i.e., the angular momenta $\boldsymbol{j}_p$, $\boldsymbol{j}_n$, and $\boldsymbol{R}$ have to cancel out to obtain the total spin zero. The sum of the three effective angles equals to ≈360°, i.e., the three angular momenta indeed lie in a plane.

The three effective angles gradually decrease with spin and drop to ≈90° at the bandhead ($I = 8\hbar$), which leads to the conclusion that the angular momenta $\boldsymbol{j}_p$, $\boldsymbol{j}_n$, and $\boldsymbol{R}$ are nearly mutually perpendicular to each other in Ref. [43]. This is the paradox with respect to the understanding of chiral vibration near the bandhead.

At the static chiral region ($15 \leqslant I \leqslant 17\hbar$), the three effective angles of the doublet bands are rather similar. Note that the values of these three effective angles are about 70°, a bit far from 90°. It seems that the aplanar rotation at this spin region is less than that near the bandhead. This is also in contradiction with our empirical understanding of the static chirality and needs to be solved.

The obvious odd-even staggering behaviors of $\theta_{pn}$ at $I \geqslant 20\hbar$ and of $\theta_{Rp/Rn}$ at $I \geqslant 21\hbar$ indicate a strong signature splitting of a principle axis rotation.

For the effective angles with respect to the total spin, $\theta_{Ip/In}$ are smaller than 90° at the whole spin region, which implies that $\boldsymbol{j}_p$ and $\boldsymbol{j}_n$ align toward the total spin. At $I \geqslant 13\hbar$, they do not vary much. For $\theta_{IR}$, it is larger than 90° for the yrast band below the bandhead. This means that the $\boldsymbol{R}$ anti-aligns along the total spin. The decreasing of $\theta_{IR}$ indicates that the role of the rotor becomes more and more essential. Meanwhile, the differences of $\theta_{Ip/In}/\theta_{IR}$ between the doublet bands become smaller with spin. At $I = 15$–$17\hbar$, they are almost the same. At the high spin region ($I > 20\hbar$), $\theta_{Ip/In}/\theta_{IR}$ show small staggering behaviors.

To solve this paradox, we first reexamine the energy spectra of the chiral doublet bands in Fig. 2(a). Similar results have already been presented in Refs. [1,15,22,35], but here we will focus on the lower spin (from $0\hbar$) ones. At $I \leqslant 8\hbar$, the energies of the doublets decrease with spin, since the collective rotations have not yet started. In Fig. 2, the dashed-dotted line at $I = 8\hbar$ is plotted to label this bandhead position. At the intermediate spin region (around $I = 15$–$17\hbar$), near energy degeneracies of doublets are found. To show this more clearly, the energy difference between the doublet bands $\Delta E(I) = E_{\text{yrare}}(I) - E_{\text{yrast}}(I)$ is shown in Fig. 2(c). One sees that it decreases first and then increases. At $I = 15$–$17\hbar$, it is the smallest, corresponding to the best degeneracy and static chirality (marked by a shadow). At the high spin region

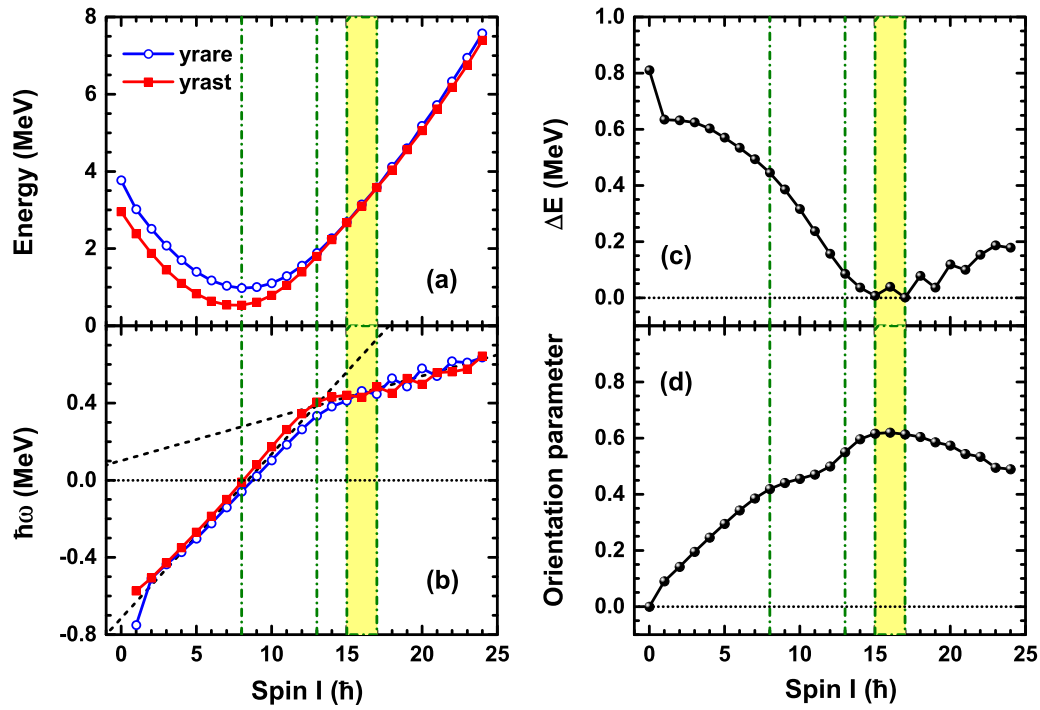


FIG. 2. (a) Energy spectra as functions of spin for the yrast and yrare bands. (b) Extracted rotational frequencies as functions of spin. (c) Energy difference between the doublets. (d) Normalized orientation parameter calculated by Eq. (2).

($I \geqslant 18\hbar$), it shows an odd-even staggering behavior, caused by the signature splitting in the transition process from the chiral to principal axis rotation.

From the energy spectra, the rotational frequencies $\hbar\omega(I) = E(I) - E(I-1)$ are extracted [57] and shown in Fig. 2(b). It is seen that the $\hbar\omega$ increases with spin.

Below the bandhead ($I < 8\hbar$), $\hbar\omega$ is negative. This indicates the angular momentum of the rotor anti-aligns along the spin, which is consistent with the results of $\theta_{IR}$ shown in Fig. 1(b).

At the bandhead, $\hbar\omega$ is near zero. The collective rotation is just starting and rather small.

At $I = 13\hbar$, a kink appears. As discussed in Ref. [1], this is evidence of the onset of the aplanar rotation. A dashed-dotted line is plotted to label this position. Note that the spin region ($8 \leqslant I < 13\hbar$) from the bandhead to the kink are usually

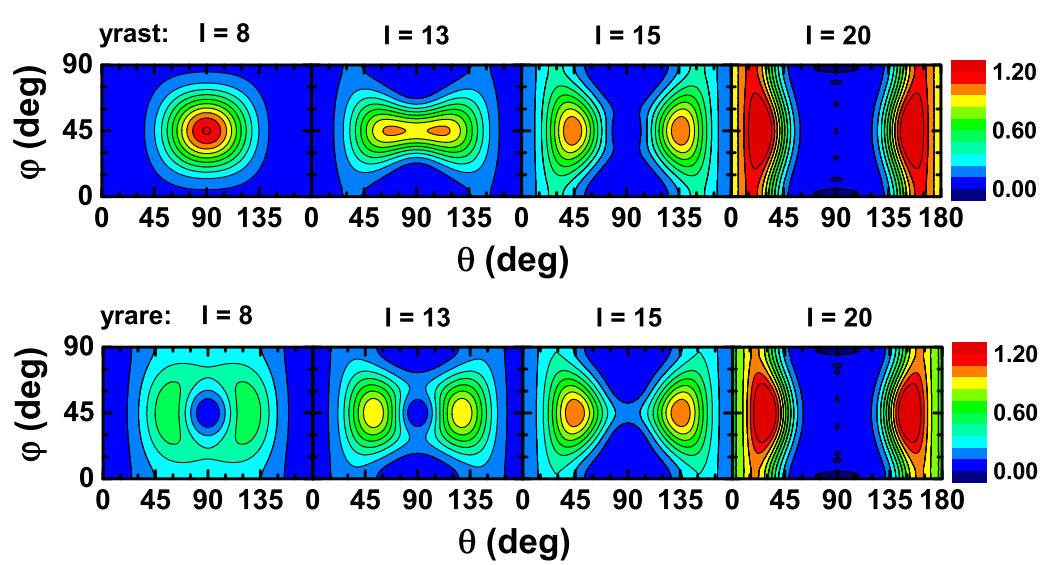


FIG. 3. Azimuthal plots, i.e., profiles for the orientation of the angular momentum on the $(\theta, \varphi)$ plane, calculated at $I = 8$, 13, 15, and $20\hbar$, for the yrast and yrare bands.

called the chiral vibration region, which in fact is a planar rotation [1,23,31,32].

At $I = 15$–$17\hbar$, the spin region of the best degeneracy of the doublets, the $\hbar\omega$ of the doublet bands are very similar. This gives a hint that the angular momentum geometries of the doublets are similar.

To examine the angular momentum coupling modes of the system, the normalized orientation parameter $o$ is calculated [41,42]:

$$o = \frac{\langle\mathcal{L}|\boldsymbol{R}\cdot(\boldsymbol{j}_p\times\boldsymbol{j}_n)|\mathcal{L}\rangle}{\sqrt{\langle\mathcal{L}|\boldsymbol{j}_p^2|\mathcal{L}\rangle}\sqrt{\langle\mathcal{L}|\boldsymbol{j}_n^2|\mathcal{L}\rangle}\sqrt{\langle\mathcal{L}|\boldsymbol{R}^2|\mathcal{L}\rangle}}, \tag{2}$$

with $\langle\mathcal{L}|\boldsymbol{R}\cdot(\boldsymbol{j}_p\times\boldsymbol{j}_n)|\mathcal{L}\rangle = |\langle+|\boldsymbol{R}\cdot(\boldsymbol{j}_p\times\boldsymbol{j}_n)|-\rangle|$ and $\langle\mathcal{L}|\boldsymbol{j}^2|\mathcal{L}\rangle = \frac{1}{2}[\langle+|\boldsymbol{j}^2|+\rangle + \langle-|\boldsymbol{j}^2|-\rangle]$ ($\boldsymbol{j}$ denotes $\boldsymbol{j}_p$, $\boldsymbol{j}_n$, and $\boldsymbol{R}$). Here, $|+\rangle$ and $|-\rangle$ denote the wave functions of yrast and yrare bands, and $|\mathcal{L}\rangle$ the wave function of left-handed state in the intrinsic frame. In classical mechanics, the normalized orientation parameter would vary between $o = 1$ for mutually perpendicular vectors and $o = 0$ for planar vectors [41,42].

The result of the normalized orientation parameter was given for the static chirality [41,42] or for the bandhead [23]. Here we present it for the whole spin region in Fig. 2(d).

At $I = 0$, $o = 0$. This indicates a planar angular momentum geometry and is consistent with the result that the effective angles $\theta_{pn}$, $\theta_{Rp}$, and $\theta_{Rn}$ are about 120° [cf. Fig. 1(a)].

With the increase of spin, $o$ first increases and then decreases, corresponding to the appearance and disappearance of the aplanar rotation. It shows strong correlation with the energy difference $\Delta E$ of the doublet bands [cf. Fig. 2(c)]. At $I = 15$–$17\hbar$, $o$ reaches the maximal value, corresponding to the smallest $\Delta E$ and the static chirality. It is also noted that the maximal value of $o$ is not 1. This is consistent with the result that the effective angles $\theta_{Rp}$, $\theta_{Rn}$, and $\theta_{pn}$ are not 90° at this spin region as shown in Fig. 1(a). Hence, one concludes that the angular momenta of the rotor, proton particle, and neutron hole are not ideally mutually perpendicular to each other at the static chiral region. Nevertheless, the aplanar angular momentum geometry at the static chiral region is better than that near the bandhead.

The angular momentum geometry can also be illustrated by its profile on the $(\theta,\varphi)$ plane $\mathcal{P}(\theta,\varphi)$, i.e., the azimuthal plot [39,40]. Here, $(\theta,\varphi)$ are the tilted angles of the total angular momentum with respect to the intrinsic reference frame. In the calculations, 1, 2, and 3 axes are chosen as short ($s$), long ($l$), and intermediate ($i$) axes of the deformed body, respectively. In Refs. [39,40], the axes with (1,2,3) = ($s$, $i$, $l$) have been employed. In the following, one can see that because of the present choice, the interpretation of the azimuthal plot is much clearer.

In Fig. 3, the obtained profiles $\mathcal{P}(\theta,\varphi)$ are shown at $I =$ 8, 13, 15, and $20\hbar$ for the doublet bands. It is observed that the maxima of the $\mathcal{P}(\theta,\varphi)$ always locate at $\varphi = 45°$ for all cases, since the angular momentum has the same distributions along the $s$ and $l$ axes for the current symmetric particle-hole configuration with triaxial deformation $\gamma = 30°$. In addition, $\mathcal{P}(\theta,\varphi)$ is symmetric with respect to the $\theta = 90°$ line. This is expected since the broken chiral symmetry in the intrinsic reference frame has been fully restored in the PRM wave functions. Hence, in the following, only the value of $\theta$ ($\leqslant 90°$) is given when mentioning the position of the maximal $\mathcal{P}(\theta,\varphi)$.

For the bandhead $I = 8\hbar$, the angular momentum for the yrast band mainly orientates at $\theta = 90°$, namely, a planar rotation within the $s$-$l$ plane. The angular momentum for the yrare band orientates at $\theta \approx 60°$, in accordance with the interpretation of chiral vibration along the $\theta$ direction (i.e., with respect to the $s$-$l$ plane). For $I = 13\hbar$, the angular momenta orientate at $\theta \approx 70°$ for the yrast band and $\theta \approx 50°$ for the yrare band. Starting from this spin, the rotational mode of the yrast band changes from planar to aplanar rotation. This is consistent with the appearance of a kink in the rotational frequency plot shown in Fig. 2(b). For $I = 15\hbar$, the $\mathcal{P}(\theta,\varphi)$ of the yrast and yrare bands are rather similar, which demonstrates the occurrence of static chirality. The angular momenta orientate at $\theta \approx 45°$ for both bands. For $I = 20\hbar$, the static chirality disappears. The angular momentum for the yrast band orientates to $\theta \approx 20°$, while that for the yrare band to $\theta \approx 30°$. The small values of $\theta$ correspond to the fact that the angular momentum has a large component along the $i$ axis.

Therefore, from the investigations of the azimuthal plots in Fig. 3, we confirm that the rotational mode at bandhead is indeed a planar rotation. Then, how do we understand the results that the effective angles $\theta_{pn}$, $\theta_{Rp}$, and $\theta_{Rn}$ are about 90°? We turn to investigating the vector lengths of the angular momenta.

The angular momenta of the rotor, proton particle, and neutron hole are coupled to obtain the total spin as $\boldsymbol{I} = \boldsymbol{R} + \boldsymbol{J}$ with $\boldsymbol{J} = \boldsymbol{j}_p + \boldsymbol{j}_n$. As a consequence, $\boldsymbol{I}^2$ can be decomposed as

$$\boldsymbol{I}^2 = \boldsymbol{R}^2 + \left(\boldsymbol{j}_p^2 + \boldsymbol{j}_n^2\right) + 2\boldsymbol{R}\cdot\boldsymbol{J} + 2\boldsymbol{j}_p\cdot\boldsymbol{j}_n. \tag{3}$$

The ratios $\langle\boldsymbol{R}^2\rangle/\langle\boldsymbol{I}^2\rangle$, $\langle\boldsymbol{j}_p^2 + \boldsymbol{j}_n^2\rangle/\langle\boldsymbol{I}^2\rangle$, $\langle 2\boldsymbol{R}\cdot\boldsymbol{J}\rangle/\langle\boldsymbol{I}^2\rangle$, and $\langle 2\boldsymbol{j}_p\cdot\boldsymbol{j}_n\rangle/\langle\boldsymbol{I}^2\rangle$ (labeled as $\mathrm{R}_{R^2}$, $\mathrm{R}_{j^2}$, $\mathrm{R}_{R*j}$, $\mathrm{R}_{j_p*j_n}$, respectively) as functions of spin for the doublet bands are calculated and shown in Fig. 4(a). Obviously, the sum of these four ratios are equal to 1.

From Fig. 4(a), it is seen that $\mathrm{R}_{j^2}$ decreases in a hyperbola-like behavior, since $\langle\boldsymbol{j}_p^2 + \boldsymbol{j}_n^2\rangle = j_p(j_p+1) + j_n(j_n+1)$ is a constant in the single-$j$ shell model, while $\langle\boldsymbol{I}^2\rangle = I(I+1)$ increases in terms of $I^2$. For the others, the $\mathrm{R}_{R*j}$ increases gradually, the $\mathrm{R}_{j_p*j_n}$ first increases and then keeps nearly constant above the bandhead, and the $\mathrm{R}_{R^2}$ first decreases and then increases.

In detail, both the $\mathrm{R}_{R*j}$ and the $\mathrm{R}_{j_p*j_n}$ give negative contributions below the bandhead. At the bandhead, the $\mathrm{R}_{j_p*j_n}$ is zero, and above the bandhead, its contribution to the total spin is rather small. For the $\mathrm{R}_{j^2}$, its contribution is much larger than 1 below the bandhead. At the chiral vibration region ($8 \leqslant I < 13\hbar$), it still has a major contribution ($\geqslant$40%) to the total spin. At the static chiral region, its contribution is similar as those of $\mathrm{R}_{R^2}$ and $\mathrm{R}_{R*j}$. However, beyond this region, it becomes much smaller than $\mathrm{R}_{R^2}$ and $\mathrm{R}_{R*j}$. This is because the angular momentum of the rotor plays a more and more essential role than those of the particle and hole as the spin

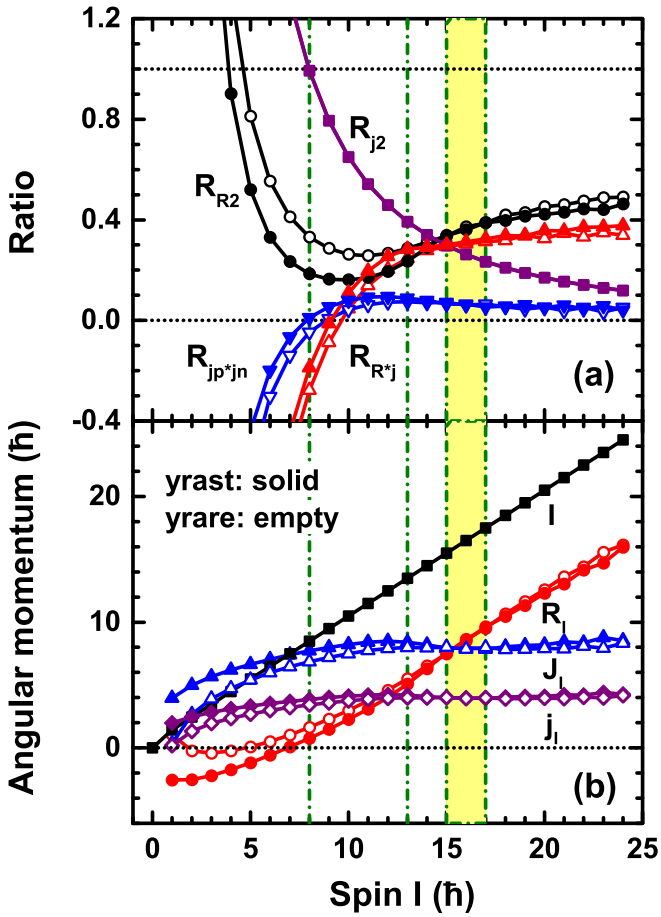


FIG. 4. (a) Ratios $\langle \boldsymbol{R}^2\rangle/\langle \boldsymbol{I}^2\rangle$, $\langle \boldsymbol{j}_p^2+\boldsymbol{j}_n^2\rangle/\langle \boldsymbol{I}^2\rangle$, $\langle 2\boldsymbol{R}\cdot\boldsymbol{J}\rangle/\langle \boldsymbol{I}^2\rangle$, and $\langle 2\boldsymbol{j}_p\cdot\boldsymbol{j}_n\rangle/\langle \boldsymbol{I}^2\rangle$ (labeled as $\mathrm{R}_{R^2}$, $\mathrm{R}_{j^2}$, $\mathrm{R}_{R*j}$, $\mathrm{R}_{j_p*j_n}$, respectively) as functions of spin for the yrast and yrare bands. (b) Angular momentum vector projection along the total spin $I=\sqrt{\langle \boldsymbol{I}^2\rangle}$ of the rotor $R_I=\langle \boldsymbol{R}\cdot\boldsymbol{I}\rangle/\sqrt{\langle \boldsymbol{I}^2\rangle}$, the particles $J_I=\langle \boldsymbol{J}\cdot\boldsymbol{I}\rangle/\sqrt{\langle \boldsymbol{I}^2\rangle}$ and $j_I=\langle \boldsymbol{j}_p\cdot\boldsymbol{I}\rangle/\sqrt{\langle \boldsymbol{I}^2\rangle}=\langle \boldsymbol{j}_n\cdot\boldsymbol{I}\rangle/\sqrt{\langle \boldsymbol{I}^2\rangle}$ as functions of spin for the yrast and yrare bands.

increases. At the bandhead, the angular momentum of the rotor is rather small in comparison with those of particle and hole. As a result, although it is perpendicular to $\boldsymbol{j}_p$ and $\boldsymbol{j}_n$, it does not indicate an aplanar rotation and good chirality. Bear in mind that the total angular momentum for the yrast band still lies in the $s$-$l$ plane (cf. Fig. 3).

It is also noted that the $\mathrm{R}_{R^2}$ of the doublet bands are quite different at the chiral vibration region. This is attributed to the fact that the angular momentum of the rotor lies mainly in the $s$-$l$ plane for the yrast band, while it deviates from this plane for the yrare band in the chiral vibration region. Such differences cause the energies of the doublet bands to be different as shown in Fig. 2(c). It also provides the additional information that static chirality is not realized yet.

From the above analysis, one concludes that the total spin below the static chiral region ($I<15\hbar$) mainly comes from the proton and neutron, in the static chiral region ($15\leqslant I\leqslant 17\hbar$) also from the rotor, and beyond the static chiral region ($I>17\hbar$) mainly from the rotor. The paradox is caused by the fact that the angular momentum of the rotor is much smaller than those of proton and neutron near the bandhead. To show this more clearly, the projections of the rotor $R_I$ and the particles $J_I$ and $j_I$ along the total spin are calculated:

$$R_I=\langle \boldsymbol{R}\cdot\boldsymbol{I}\rangle/\sqrt{\langle \boldsymbol{I}^2\rangle}, \tag{4}$$

$$J_I=\langle \boldsymbol{J}\cdot\boldsymbol{I}\rangle/\sqrt{\langle \boldsymbol{I}^2\rangle}, \tag{5}$$

$$j_I=\langle \boldsymbol{j}_p\cdot\boldsymbol{I}\rangle/\sqrt{\langle \boldsymbol{I}^2\rangle}=\langle \boldsymbol{j}_n\cdot\boldsymbol{I}\rangle/\sqrt{\langle \boldsymbol{I}^2\rangle}. \tag{6}$$

Note that here $J_I=2j_I$ and $R_I+J_I=\sqrt{\langle \boldsymbol{I}^2\rangle}=\sqrt{I(I+1)}$. The obtained results are given in Fig. 4(b).

With the increase of spin, $R_I$ increases gradually. The $J_I$ as well as the $j_I$ increase slightly below the kink ($I\leqslant 13\hbar$), and keep nearly constant in the region above ($I>13\hbar$). Below the bandhead, $R_I$ contributes negatively as it anti-aligns along the total spin. At the bandhead, it is very small. Then it becomes gradually comparable with $j_I$, but is still smaller than $J_I$. At static chiral region, $R_I\approx J_I$. This is consistent with the result that the value of $\theta$ for the maximal $\mathcal{P}(\theta,\varphi)$ is about 45° (cf. Fig. 3). In this case, the energy difference between the doublet bands is the smallest. Beyond the static chiral region, $R_I$ becomes larger than $J_I$ and responsible for the increase of total spin, which results in a transition process from the chiral to principal axis rotation along the $i$ axis. Therefore, with the increase of spin, the angular momentum of the rotor plays gradually more important roles than those of the proton particle and neutron hole.

In summary, the paradox in the previous interpretation of the nuclear chiral geometry based on the effective angle has been clarified by reexamining the system with the particle-hole configuration $\pi(1h_{11/2})^1\otimes\nu(1h_{11/2})^{-1}$ and rotor with deformation parameter $\gamma=30°$. According to the studies of normalized orientation parameter of the system and the azimuthal plot of the total angular momentum, we confirm that chiral rotation does indeed exist only at a certain high spin region. Further study of the angular momentum shows that the paradox is caused by the fact that the angular momentum of the rotor is much smaller than those of the proton and neutron near the bandhead. Hence, it does not support a chiral rotation interpretation near the bandhead. The nuclear chiral geometry based on the effective angle makes sense only when the angular momentum of the rotor becomes comparable with those of the proton and the neutron for a particular range of spin values.

The authors thank S. Q. Zhang and P. W. Zhao for fruitful discussions. Financial support for this work was provided in part by Deutsche Forschungsgemeinschaft (DFG) and National Natural Science Foundation of China (NSFC) through funds provided to the Sino-German CRC 110 “Symmetries and the Emergence of Structure in QCD”, the National Key R&D Program of China (Contract No. 2018YFA0404400), and the NSFC under Grants No. 11335002 and No. 11621131001.

[1] S. Frauendorf and J. Meng, Nucl. Phys. A **617**, 131 (1997).
[2] J. Meng and S. Q. Zhang, J. Phys. G: Nucl. Part. Phys. **37**, 064025 (2010).
[3] J. Meng, Q. B. Chen, and S. Q. Zhang, Int. J. Mod. Phys. E **23**, 1430016 (2014).
[4] R. A. Bark, E. O. Lieder, R. M. Lieder, E. A. Lawrie, J. J. Lawrie, S. P. Bvumbi, N. Y. Kheswa, S. S. Ntshangase, T. E. Madiba, P. L. Masiteng *et al.*, Int. J. Mod. Phys. E **23**, 1461001 (2014).
[5] J. Meng and P. W. Zhao, Phys. Scr. **91**, 053008 (2016).
[6] A. A. Raduta, Prog. Part. Nucl. Phys. **90**, 241 (2016).
[7] K. Starosta and T. Koike, Phys. Scr. **92**, 093002 (2017).
[8] S. Frauendorf, Phys. Scr. **93**, 043003 (2018).
[9] J. Meng, J. Peng, S. Q. Zhang, and S.-G. Zhou, Phys. Rev. C **73**, 037303 (2006).
[10] A. D. Ayangeakaa, U. Garg, M. D. Anthony, S. Frauendorf, J. T. Matta, B. K. Nayak, D. Patel, Q. B. Chen, S. Q. Zhang, P. W. Zhao *et al.*, Phys. Rev. Lett. **110**, 172504 (2013).
[11] J. Peng, H. Sagawa, S. Q. Zhang, J. M. Yao, Y. Zhang, and J. Meng, Phys. Rev. C **77**, 024309 (2008).
[12] J. M. Yao, B. Qi, S. Q. Zhang, J. Peng, S. Y. Wang, and J. Meng, Phys. Rev. C **79**, 067302 (2009).
[13] J. Li, S. Q. Zhang, and J. Meng, Phys. Rev. C **83**, 037301 (2011).
[14] C. Droste, S. G. Rohozinski, K. Starosta, L. Prochniak, and E. Grodner, Eur. Phys. J. A **42**, 79 (2009).
[15] Q. B. Chen, J. M. Yao, S. Q. Zhang, and B. Qi, Phys. Rev. C **82**, 067302 (2010).
[16] I. Hamamoto, Phys. Rev. C **88**, 024327 (2013).
[17] D. Tonev, M. S. Yavahchova, N. Goutev, G. de Angelis, P. Petkov, R. K. Bhowmik, R. P. Singh, S. Muralithar, N. Madhavan, R. Kumar *et al.*, Phys. Rev. Lett. **112**, 052501 (2014).
[18] E. O. Lieder, R. M. Lieder, R. A. Bark, Q. B. Chen, S. Q. Zhang, J. Meng, E. A. Lawrie, J. J. Lawrie, S. P. Bvumbi, N. Y. Kheswa *et al.*, Phys. Rev. Lett. **112**, 202502 (2014).
[19] N. Rather, P. Datta, S. Chattopadhyay, S. Rajbanshi, A. Goswami, G. H. Bhat, J. A. Sheikh, S. Roy, R. Palit, S. Pal *et al.*, Phys. Rev. Lett. **112**, 202503 (2014).
[20] I. Kuti, Q. B. Chen, J. Timár, D. Sohler, S. Q. Zhang, Z. H. Zhang, P. W. Zhao, J. Meng, K. Starosta, T. Koike *et al.*, Phys. Rev. Lett. **113**, 032501 (2014).
[21] C. Liu, S. Y. Wang, R. A. Bark, S. Q. Zhang, J. Meng, B. Qi, P. Jones, S. M. Wyngaardt, J. Zhao, C. Xu *et al.*, Phys. Rev. Lett. **116**, 112501 (2016).
[22] H. Zhang and Q. B. Chen, Chin. Phys. C **40**, 024101 (2016).
[23] E. Grodner, J. Srebrny, C. Droste, L. Próchniak, S. G. Rohoziński, M. Kowalczyk, M. Ionescu-Bujor, C. A. Ur, K. Starosta, T. Ahn *et al.*, Phys. Rev. Lett. **120**, 022502 (2018).
[24] J. Li, Phys. Rev. C **97**, 034306 (2018).
[25] C. M. Petrache, B. F. Lv, A. Astier, E. Dupont, Y. K. Wang, S. Q. Zhang, P. W. Zhao, Z. X. Ren, J. Meng, P. T. Greenlees *et al.*, Phys. Rev. C **97**, 041304(R) (2018).
[26] B. Moon, C.-B. Moon, G. Dracoulis, R. Bark, A. Byrne, P. Davidson, G. Lane, T. Kibédi, A. Wilson, C. Yuan *et al.*, Phys. Lett. B **782**, 602 (2018).
[27] T. Roy, G. Mukherjee, M. Asgar, S. Bhattacharyya, S. Bhattacharya, C. Bhattacharya, S. Bhattacharya, T. Ghosh, K. Banerjee, S. Kundu *et al.*, Phys. Lett. B **782**, 768 (2018).
[28] B. Qi, H. Jia, C. Liu, and S. Y. Wang, Phys. Rev. C **98**, 014305 (2018).
[29] J. Peng and Q. B. Chen, Phys. Rev. C **98**, 024320 (2018).
[30] S. Frauendorf, Rev. Mod. Phys. **73**, 463 (2001).
[31] P. Olbratowski, J. Dobaczewski, J. Dudek, and W. Płóciennik, Phys. Rev. Lett. **93**, 052501 (2004).
[32] P. Olbratowski, J. Dobaczewski, and J. Dudek, Phys. Rev. C **73**, 054308 (2006).
[33] S. Q. Zhang, B. Qi, S. Y. Wang, and J. Meng, Phys. Rev. C **75**, 044307 (2007).
[34] B. Qi, S. Q. Zhang, J. Meng, S. Y. Wang, and S. Frauendorf, Phys. Lett. B **675**, 175 (2009).
[35] B. Qi, S. Q. Zhang, S. Y. Wang, J. M. Yao, and J. Meng, Phys. Rev. C **79**, 041302(R) (2009).
[36] E. A. Lawrie and O. Shirinda, Phys. Lett. B **689**, 66 (2010).
[37] C. M. Petrache, Q. B. Chen, S. Guo, A. D. Ayangeakaa, U. Garg, J. T. Matta, B. K. Nayak, D. Patel, J. Meng, M. P. Carpenter *et al.*, Phys. Rev. C **94**, 064309 (2016).
[38] J. Peng, J. Meng, and S. Q. Zhang, Phys. Rev. C **68**, 044324 (2003).
[39] F. Q. Chen, Q. B. Chen, Y. A. Luo, J. Meng, and S. Q. Zhang, Phys. Rev. C **96**, 051303 (2017).
[40] F. Q. Chen, J. Meng, and S. Q. Zhang, Phys. Lett. B **785**, 211 (2018).
[41] K. Starosta, T. Koike, C. J. Chiara, D. B. Fossan, and D. R. LaFosse, Nucl. Phys. A **682**, 375 (2001).
[42] K. Starosta, C. J. Chiara, D. B. Fossan, T. Koike, T. T. S. Kuo, D. R. LaFosse, S. G. Rohozinski, C. Droste, T. Morek, and J. Srebrny, Phys. Rev. C **65**, 044328 (2002).
[43] S. Y. Wang, S. Q. Zhang, B. Qi, and J. Meng, Phys. Rev. C **75**, 024309 (2007).
[44] P. W. Zhao, Phys. Lett. B **773**, 1 (2017).
[45] T. Koike, K. Starosta, and I. Hamamoto, Phys. Rev. Lett. **93**, 172502 (2004).
[46] Q. B. Chen, K. Starosta, and T. Koike, Phys. Rev. C **97**, 041303(R) (2018).
[47] Q. B. Chen, B. F. Lv, C. M. Petrache, and J. Meng, Phys. Lett. B **782**, 744 (2018).
[48] V. I. Dimitrov, S. Frauendorf, and F. Dönau, Phys. Rev. Lett. **84**, 5732 (2000).
[49] D. Almehed, F. Dönau, and S. Frauendorf, Phys. Rev. C **83**, 054308 (2011).
[50] Q. B. Chen, S. Q. Zhang, P. W. Zhao, R. V. Jolos, and J. Meng, Phys. Rev. C **87**, 024314 (2013).
[51] Q. B. Chen, S. Q. Zhang, P. W. Zhao, R. V. Jolos, and J. Meng, Phys. Rev. C **94**, 044301 (2016).
[52] S. Brant, D. Tonev, G. de Angelis, and A. Ventura, Phys. Rev. C **78**, 034301 (2008).
[53] G. H. Bhat, J. A. Sheikh, and R. Palit, Phys. Lett. B **707**, 250 (2012).
[54] G. H. Bhat, R. N. Ali, J. A. Sheikh, and R. Palit, Nucl. Phys. A **922**, 150 (2014).
[55] M. Shimada, Y. Fujioka, S. Tagami, and Y. R. Shimizu, Phys. Rev. C **97**, 024319 (2018).
[56] J. Meng, ed., *Relativistic Density Functional for Nuclear Structure*, Vol. 10, *International Review of Nuclear Physics* (World Scientific, Singapore, 2016).
[57] S. Frauendorf and J. Meng, Z. Phys. A **356**, 263 (1996).